Rakenteiden Mekaniikka (Journal of Structural Mechanics)
Vol. 44, No 3, 2011, pp. 279 – 291

Accuracy assessment of the Cartesian grid method for compressible inviscid flows using a simplified ghost point treatment

M. Asif Farooq and B. Müller

Summary. We introduce a new approach to treat ghost points near embedded boundaries to solve the 2D compressible Euler equations on a Cartesian grid. Solid wall boundary conditions are imposed by our new approach called simplified ghost point treatment for compressible inviscid flows with embedded boundaries. In the simplified ghost point treatment, we assume the solid boundary to lie in the middle between two grid points in the y-direction. Symmetry conditions are used to determine density, pressure, wall tangential, and wall normal velocity components at the ghost points. A cell-vertex finite volume formulation has been used to calculate transonic internal flows over a circular arc bump in a channel.

Key words: compressible Euler equations, Cartesian grid method, simplified ghost point treatment, cell-vertex finite volume method

Introduction

In Computational Fluid Dynamics (CFD) two methods are popular in the scientific community. One is the standard body fitted grid method and the other is the Cartesian grid method. In the former solid boundaries and grid lines conform to each other but in the latter this is not the case. Standard body fitted grid methods both with structured and unstructured grids successfully solved many complex problems in the past [1–4]. But these methods involve a numerical complexity which is sometime discouraging for the scientific community. The popularity of the Cartesian grid method [5–9] is due to its simplicity, faster grid generation, simpler programming, lower storage requirements, lower operation count, and easier post processing compared to body fitted structured and unstructured grid methods. The Cartesian grid method is also advantageous in constructing higher order methods. A disadvantage of this method shows up when it is applied to complex domains. At curved boundaries the cells are not rectangular and these cut-cells create a problem in time-stepping for a scheme to be implemented. The solution to this cut-cell problem is to merge these cut-cells with neighboring cells. The main disadvantage of the cut-cell approach is the complexity of the method in which fluxes are calculated at the interfaces near the embedded boundary.

We avoided the cut-cell approach [10] and opt for the ghost point treatment at the boundary [11]. The main motivation has been the simplicity of the ghost point treatment over the more complicated cut-cell approach. The advantage of the present simplified ghost point approach resides in its ability of implementing the method with ease and extending it to a higher order method. In the ghost point treatment, we divide our

domain into three types of points: fluid, ghost and solid points. Only fluid and ghost points are treated in the scheme, and solid points are cut out of the present computation.

In [11] we successfully compared supersonic external flow results over a circular arc airfoil with standard body fitted grid results. In this paper, we further analyse the simplified ghost point treatment for the 2D compressible Euler equations to simulate transonic internal flow. In the simplified ghost point treatment, we assume the solid boundary to lie in the middle between two grid points in the y-direction. Our assumption is based on the fact that the normal to the wall boundary in slender bodies can be assumed to lie in the y-direction. Symmetry conditions are used to determine density, pressure, wall tangential, and wall normal velocity components at the ghost points. We employ the local Lax-Friedrichs (lLF) method for the spatial discretization. The local Lax-Friedrichs method is chosen over other numerical methods like Roe's method because of its simplicity. We apply the Monotone Upstream-centered Schemes for Conservation Laws (MUSCL) approach with the minmod limiter to get a second order method except for extrema. For time integration we use the third order Total Variation Diminishing Runge-Kutta (TVD RK3) method with the MUSCL approach. As a test case, we consider transonic internal flow over a circular arc bump in a channel and solve the 2D compressible Euler equations by time stepping to the steady state. We compute a shock in the channel with the circular arc bump and compare these results with the results presented in the literature. We need a larger number of grid points than standard body fitted grid methods to obtain results comparable with [12].

In the following section, we discuss the governing equations, i.e. for 2D compressible Euler equations. In the next sections, we outline Boundary conditions, Discretization and Approximation of boundary conditions. Simplified ghost point treatment and Results are discussed in the next two sections. Conclusions are drawn at the end.

2D compressible Euler equations

The 2D compressible Euler equations in conservative form read

$$\frac{\partial U}{\partial t} + \frac{\partial F}{\partial x} + \frac{\partial G}{\partial y} = 0, \tag{1}$$

where

$$U = \begin{bmatrix} \rho \\ \rho u \\ \rho v \\ \rho E \end{bmatrix}, F = \begin{bmatrix} \rho u \\ \rho u^2 + p \\ \rho uv \\ (\rho E + p)u \end{bmatrix}, G = \begin{bmatrix} \rho v \\ \rho uv \\ \rho v^2 + p \\ (\rho E + p)v \end{bmatrix}, \tag{2}$$

with ρ, u, v, E, and p denoting density, velocity components in x and y-directions, total energy per unit mass and pressure, respectively. We employ the equation of state for perfect gas

$$p = (\gamma - 1)(\rho E - \frac{1}{2}\rho(u^2 + v^2)), \tag{3}$$

where γ is the ratio of specific heats. We consider $\gamma = 1.4$ for air.

Boundary conditions

We consider the following boundaries: (1) subsonic inflow, (2) Subsonic outflow and (3) lower and upper wall. At the subsonic inflow $x = x_a$ in Fig. 1, three flow variables,

e.g. total enthalpy, entropy and velocity component v, are given as Dirichlet boundary conditions and one numerical boundary condition is used. At the subsonic outflow $x = x_b$, we prescribe one Dirichlet boundary condition, e.g. atmospheric pressure, and three numerical boundary conditions. The straight parts of the lower and upper walls are treated as symmetry boundaries. Symmetry boundary conditions near $y = y_c$ imply:

$$(\rho, \rho u, \rho E)(x, y_c + y, t) = (\rho, \rho u, \rho E)(x, y_c - y, t)$$

and

$$\rho v(x, y_c + y, t) = -\rho v(x, y_c - y, t)$$

Similar symmetry boundary conditions are imposed near $y = y_d$. On the curved part of the lower wall, local symmetry boundary conditions with respect to the wall are employed.

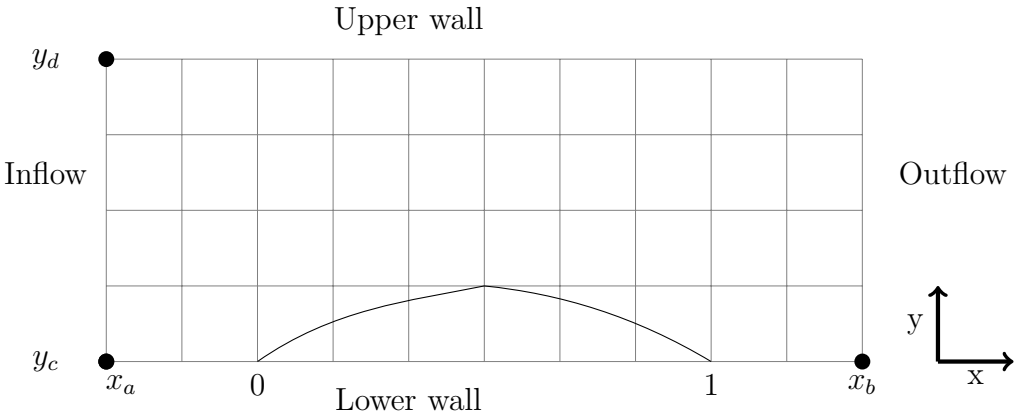

Figure 1. Computational domain and Cartesian grid for channel flow with a circular arc bump.

Discretization

Spatial discretization

We assume Cartesian coordinates (x, y), where $x_a \leq x \leq x_b$, $y_c \leq y \leq y_d$ and a Cartesian grid with $(N_x + 1) \times (N_y + 1)$ grid points. The grid points of the Cartesian coordinates are denoted by (x_i, y_j), where $x_i = x_a + i\Delta x$, with $i = 0, 1, ..., N_x$, $\Delta x = (x_b - x_a)/N_x$ and $y_j = y_c + j\Delta y$, with $j = 0, 1, ..., N_y$, $\Delta y = (y_d - y_c)/N_y$. The semi-discretization of the 2D compressible Euler equations (1) yields the following form

$$\frac{\mathrm{d}U_{i,j}}{\mathrm{d}t} = -\frac{F_{i+\frac{1}{2},j} - F_{i-\frac{1}{2},j}}{\Delta x} - \frac{G_{i,j+\frac{1}{2}} - G_{i,j-\frac{1}{2}}}{\Delta y}. \tag{4}$$

$U_{i,j}$ is the approximation of the average of U in the cell $\Omega_{i,j} = [x_i - \Delta x/2, x_i + \Delta x/2] \times [y_j - \Delta y/2, y_j + \Delta y/2]$, i.e.

$$U_{i,j} \approx \frac{1}{\Delta x \Delta y} \int_{\Omega_{i,j}} U(x, y, t) \quad dxdy. \tag{5}$$

Thus, we have been using the cell-vertex finite volume method. We opted for this approach to have a conservative method with the unknowns at the grid points. In (4), $F_{i+\frac{1}{2},j}$ and

$G_{i,j+\frac{1}{2}}$ are numerical fluxes for the 2D compressible Euler equations and $U_{i,j}$ is also an approximation of the exact solution $U(x_i, y_j, t)$. The numerical fluxes $F_{i+\frac{1}{2},j}$ and $G_{i,j+\frac{1}{2}}$ are chosen as the local Lax-Friedrichs method for F and G, which are defined as follows

$$F^{lLF}_{i+\frac{1}{2},j} = \frac{1}{2}\left[F(U_{i,j}) + F(U_{i+1,j}) - \max(|u_{i+1,j}| + c_{i+1,j}, |u_{i,j}| + c_{i,j})(U_{i+1,j} - U_{i,j})\right], \quad (6)$$

$$G^{lLF}_{i,j+\frac{1}{2}} = \frac{1}{2}\left[G(U_{i,j}) + G(U_{i,j+1}) - \max(|v_{i,j+1}| + c_{i,j+1}, |v_{i,j}| + c_{i,j})(U_{i,j+1} - U_{i,j})\right], \quad (7)$$

where c is the speed of sound. Our choice of the local Lax-Friedrichs method has been motivated by the simplicity of its numerical flux functions (6) and (7) and its total variation diminishing (TVD) property for scalar conservation laws with convex flux functions. The time step restriction of the 2D compressible Euler equations is related to the Courant-Friedrichs-Levy (CFL) number. The CFL number is defined as

$$CFL = \Delta t \quad \max_{i,j}\left(\frac{\mathrm{sp}(A_1(U_{i,j}))}{\Delta x} + \frac{\mathrm{sp}(A_2(U_{i,j}))}{\Delta y}\right), \quad (8)$$

where $\mathrm{sp}(A_1(U_{i,j}))$ and $\mathrm{sp}(A_2(U_{i,j}))$ are the spectral radii of the Jacobian matrices $A_1 = \partial F(U)/\partial U$ and $A_2 = \partial G(U)/\partial U$, respectively. We choose $CFL = 0.5$ for the results of the 2D compressible Euler equations. In (6) we replace $U_{i,j}$ by $U^L_{i+\frac{1}{2},j}$ and $U_{i+1,j}$ by $U^R_{i+\frac{1}{2},j}$ using the MUSCL [13] approach with the minmod limiter to obtain higher order accuracy and also to avoid undesired oscillations. The extrapolated variables are defined as

$$U^L_{i+\frac{1}{2},j} = U_{i,j} + \frac{1}{2}\mathrm{minmod}(U_{i,j} - U_{i-1,j}, U_{i+1,j} - U_{i,j}), \quad (9)$$

$$U^R_{i+\frac{1}{2},j} = U_{i+1,j} - \frac{1}{2}\mathrm{minmod}(U_{i+2,j} - U_{i+1,j}, U_{i+1,j} - U_{i,j}), \quad (10)$$

where

$$\mathrm{minmod}(a,b) = \begin{cases} a & \text{if} \quad |a| \le |b| \quad \text{and} \quad ab > 0 \\ b & \text{if} \quad |b| < |a| \quad \text{and} \quad ab > 0 \\ 0 & \text{if} \quad ab \le 0 \end{cases} \quad (11)$$

$$= \mathrm{sign}(a)\max\{0, \min\{|a|, \mathrm{sign}(a)b\}\}$$

is the minmod limiter. The MUSCL approach is applied similarly to the numerical fluxes $G_{i,j+\frac{1}{2}}$ in (7).

Temporal Discretization

We choose the TVD RK3 method because it has a favorable stability domain. The TVD RK3 method [14] is given as

$$\begin{aligned} \mathbf{U}^{(1)} &= \mathbf{U}^n + \Delta t\mathbf{R}(U^n), \\ \mathbf{U}^{(2)} &= \frac{3}{4}\mathbf{U}^n + \frac{1}{4}\mathbf{U}^{(1)} + \frac{1}{4}\Delta t\mathbf{R}(U^{(1)}), \\ \mathbf{U}^{(n+1)} &= \frac{1}{3}\mathbf{U}^n + \frac{2}{3}\mathbf{U}^{(2)} + \frac{2}{3}\Delta t\mathbf{R}(U^{(2)}). \end{aligned} \quad (12)$$

where $R_{i,j} = -(F_{i+\frac{1}{2},j} - F_{i-\frac{1}{2},j})/\Delta x - (G_{i,j+\frac{1}{2}} - G_{i,j-\frac{1}{2}})/\Delta y$ is the residual of the 2D compressible Euler equations define in equation (4).

Approximation of boundary conditions

The inflow and outflow boundary conditions for internal subsonic flow are imposed by means of the local Lax-Friedrichs method (6) at the edge $(1+\frac{1}{2}, j)$ and $(N_x - \frac{1}{2}, j)$, respectively. Since the flow at the inlet is subsonic, there is one characteristic curve (the left going Mach line with an acoustic wave) coming from the interior and two characteristics (the pathline with the entropy and vorticity waves and the right going Mach line with an acoustic wave) are entering from the exterior. Therefore, we need one numerical and three physical boundary conditions. But at the inlet we simply use freestream variables $U_{1,j}(t) = U_\infty$ and let the approximate Riemann solver determine a flux approximation (6) with the correct wave information at the cell face $(1+\frac{1}{2}, j)$ between the boundary point $(1, j)$ and its eastern neighbor $(2, j)$ [15]. At the outlet the flow is subsonic and two characteristics are leaving the domain from the interior and one characteristic curve is entering from outside of the domain. So we need three numerical boundary conditions and one physical boundary condition. As before, we use freestream boundary conditions at the outlet $U_{N_x,j}(t) = U_\infty$ and let the approximate Riemann solver determine a flux approximation (6) with the correct wave information at the cell face $(N_x - \frac{1}{2}, j)$ between the boundary point (N_x, j) and its western neighbor $(N_x - 1, j)$ [15]. Since the ingoing characteristic variables at inlet and outlet are unchanged, the computation of the numerical fluxes at the adjacent cell faces is based on 1D non-reflecting boundary conditions in the x-direction [15]. In summary we use the following numerical boundary conditions at $x = x_a$

$$U_{1,j}(t) = U_\infty, \tag{13}$$

and at $x = x_b$

$$U_{N_x,j}(t) = U_\infty. \tag{14}$$

We emphasize that the uniform flow conditions (13) and (14) at $x = x_a$ and $x = x_b$, respectively, are not considered to be the natural boundary conditions, but suitable flow conditions to get the numerical fluxes approximately correct at the adjacent cell faces, cf. the discussion above. The symmetry boundary conditions are implemented by considering an extra line below $y = y_c$. There we use

$$U_{i,1}(t) = \mathrm{diag}(1, 1, -1, 1) U_{i,3}(t). \tag{15}$$

The symmetry boundary conditions are also implemented at an extra line above $y = y_d$ where we use

$$U_{i,Ny+1}(t) = \mathrm{diag}(1, 1, -1, 1) U_{i,Ny-1}(t). \tag{16}$$

Simplified ghost point treatment at embedded boundary

In Fig. 2 we show the flagging strategy. We flag the ghost and solid points by assigning them 0 and -1 values, respectively. The fluid points are assigned values equal to 1. In Fig. 3 we show a simplified ghost point treatment at the solid boundary [11]. A ghost point is denoted by G. In the simplified ghost point treatment we consider the fluid point F on the vertical grid line through G adjacent to the boundary as the mirror point. Then, we assume the boundary is in the middle between ghost and fluid points. The density ρ, pressure p, and the tangential velocity component at the ghost point are symmetric with respect to the solid boundary and therefore directly determined by their values at

F. The normal velocity component u_n at the ghost point is anti-symmetric and thus gets the negative value of u_n at F. The mathematical description of this strategy is given as

$$\rho_G = \rho_F, p_G = p_F, u_G = u_F - 2(n_1 u_F + n_2 v_F)n_1, v_G = v_F - 2(n_1 u_F + n_2 v_F)n_2, \quad (17)$$

where n_1 and n_2 are the x-and y-components of the outer unit normal $\mathbf{n}$ of the boundary at the intersection with the grid line between F and G.

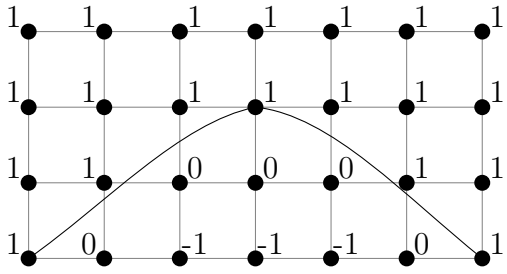

Figure 2. Flagging strategy for fluid (1), ghost (0) and solid points (-1).

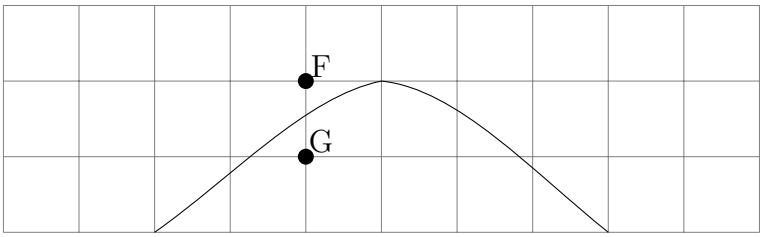

Figure 3. Simplified ghost point treatment over a circular arc bump.

If the embedded solid boundary is in the middle between ghost point G and fluid point F, then the expected normal velocity component at the solid boundary wall (index w below) is zero because the ghost point treatment (17) yields:

$$(u_n)_w = \frac{1}{2}((u_n)_F + (u_n)_G) = 0. \quad (18)$$

If the embedded solid boundary is not in the middle between G and F as in Fig. 4, we do not get zero for the arithmetic average of the normal velocity components, but

$$(u_n)_w = \frac{1}{2}((u_n)_F + (u_n)_G) = (u_n)_F(1 - \frac{2(y_F - y_w)}{\Delta y}). \quad (19)$$

So, we get an error of order $O(y_F - y_w) = O(\Delta y)$, unless $y_F - y_W = \Delta y/2$ when (19) corresponds to (18). For the tangential velocity component, density and pressure, we get for the arithmetic averages at the solid boundary wall, e.g. for pressure, from the ghost point treatment (17)

$$p_w = \frac{1}{2}(p_F + p_G) = p_F. \quad (20)$$

Using Taylor's expansion around the wall, we get

$$p_F = (p_w)_{exact} + O(y_F - y_w) = (p_w)_{exact} + O(\Delta y) \quad (21)$$

Thus with (20) and (new formula for p_F), we see that the simplified ghost point treatment (17) leads to a first order approximation at the embedded solid boundary when assuming that the boundary valves are described by the arithmetic averages at the ghost and fluid points. We see that the normal velocity component is only zero, if the embedded boundary is in the middle between ghost and fluid points.

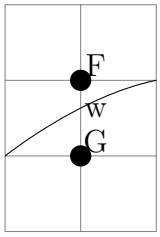

Figure 4. Detail of simplified ghost point treatment near embedded boundary.

Results

Subsonic flow in a channel with a circular arc bump flows from left to right. We use the CFL number 0.5 and 241 × 241 grid points. We assume the lengths of the domain in x-and y-directions are $x_b - x_a = 3$ m and $y_d - y_c = 1$ m, respectively. The height of the circular arc bump is 10 % of its chord length which is assumed to be 1 m. The subsonic upstream flow conditions are chosen as

$$M_\infty = 0.7, \quad p_\infty = 140510 \quad \text{Pa}, \quad T_\infty = 316.2240 \quad \text{K} \tag{22}$$

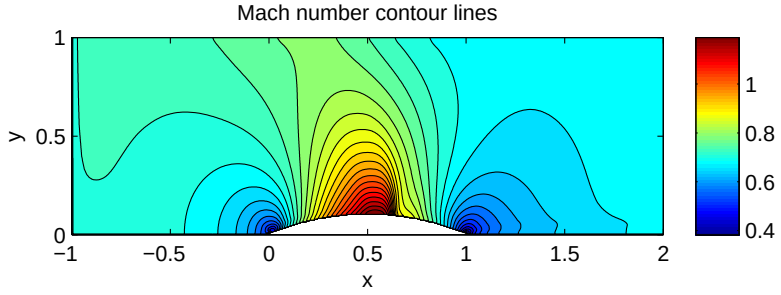

Figure 5. Mach number contours for channel flow over a circular arc bump with 241 × 241 grid points.

In Fig. 5 and Fig. 6, we compare the Mach number contours for internal flow over the circular arc bump with Hirsch [12]. In Fig. 5, we clearly see a shock wave near the downward slope of the circular arc bump. We also see that the our results are lower than Hirsch's results with a structured 65 × 33 grid. The subsonic region in our result shown in Fig. 5 is smaller and further upstream than Hirsch's result in Fig. 6. The reason for getting lower Mach numbers and the supersonic region and the shock wave shifted in the upstream direction is probably due to a relatively coarser grid. As we have shown in [11], we need a larger number of grid points compared to body-fitted grid methods. This observation is also confirmed by the results presented in the literature [6]. Probably,

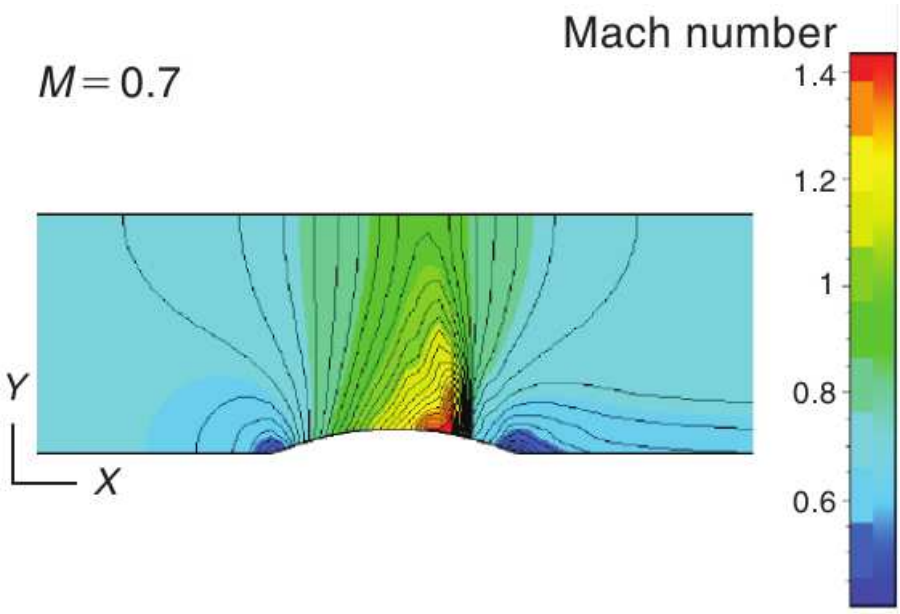

Figure 6. Mach number contours for channel flow over a circular arc bump from [12].

we could have achieved more accurate and thus less diffusive results with fewer grid points by using e.g. Roe's method instead of the local Lax-Friedrichs method (6) and (7).

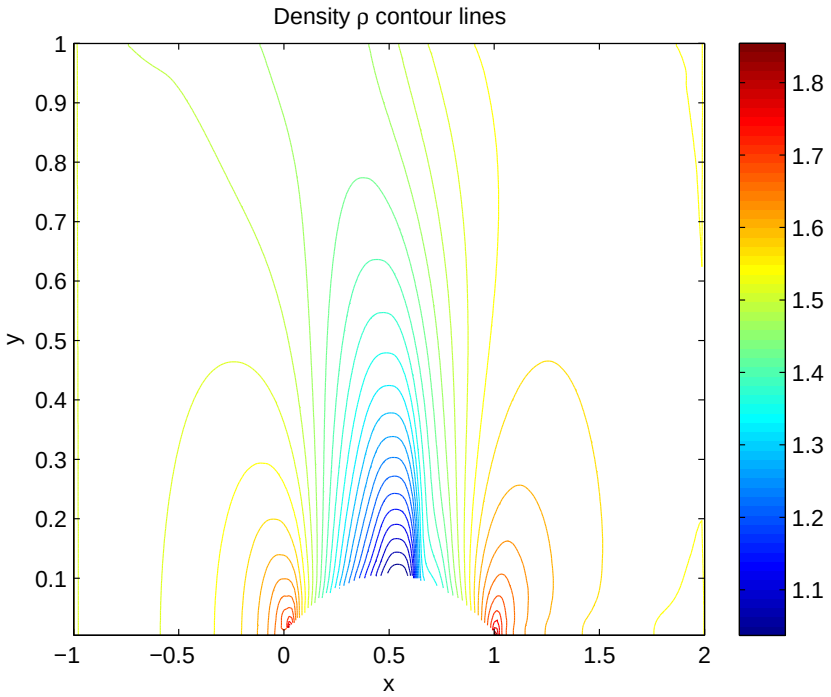

Figure 7. Density contours for channel flow over a circular arc bump with 241 × 241 grid points.

In Figs. 7, 8 and 9, we present the density ρ, velocity component u and pressure p contours for internal flow over the circular arc bump. In Figs. 7, 8 and 9, we see again the shock wave near the downward slope of the circular arc bump. The convergence history for our method based on the local Lax-Friedrichs method, MUSCL and TVD RK3 is

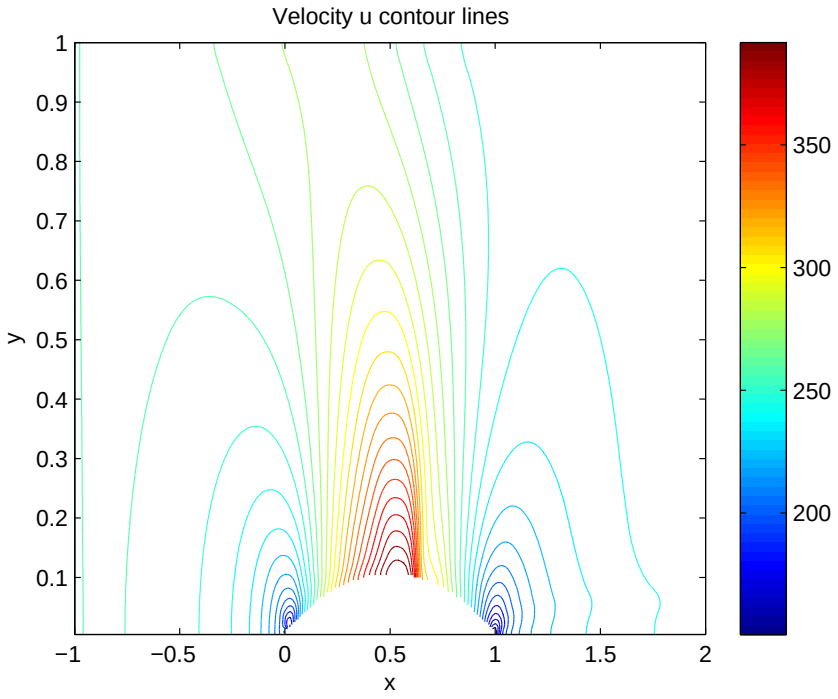

Figure 8. Velocity component u contours for channel flow over a circular arc bump with 241 × 241 grid points.

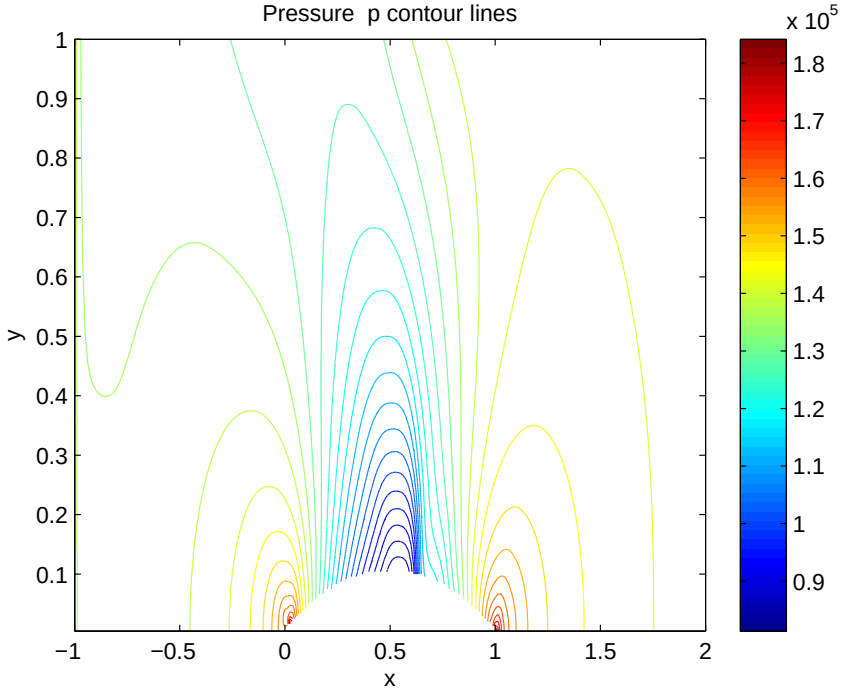

Figure 9. Pressure contours for channel flow over a circular arc bump with 241 × 241 grid points.

presented in Fig. 10. For the current results with the 241 × 241 grid, the steady state is reached at $n = 20000$. The steady state is reached at around $n = 10000$ for the 121 × 121 grid (not shown).

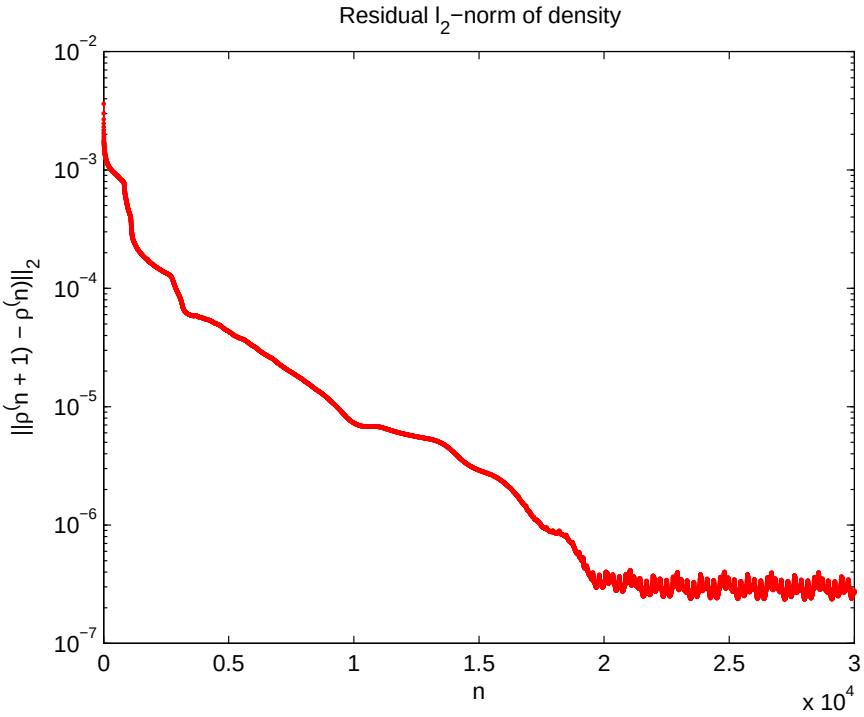

Figure 10. Residual of density for channel flow over a circular arc bump with 241 × 241 grid points.

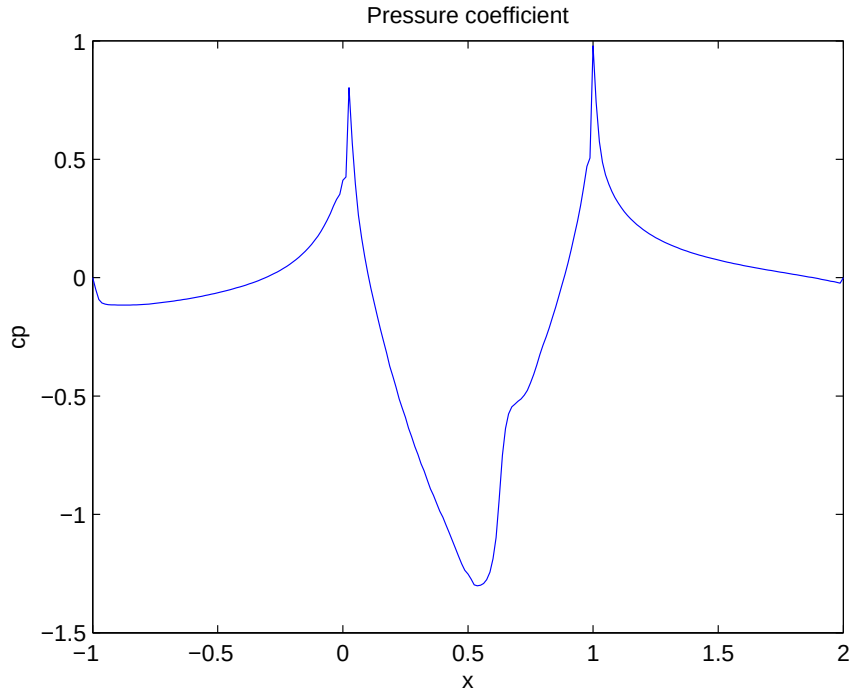

Figure 11. Pressure coefficient for channel flow over a circular arc bump with 241 × 241 grid points at $y = 0$ and on the bump surface.

In Fig. 11, we show the pressure coefficient c_p for internal flow over the circular arc bump on the x-axis $y = 0$ and on the bump surface. The pressure increases from the inflow boundary to the leading edge of the circular arc bump. The pressure decreases due

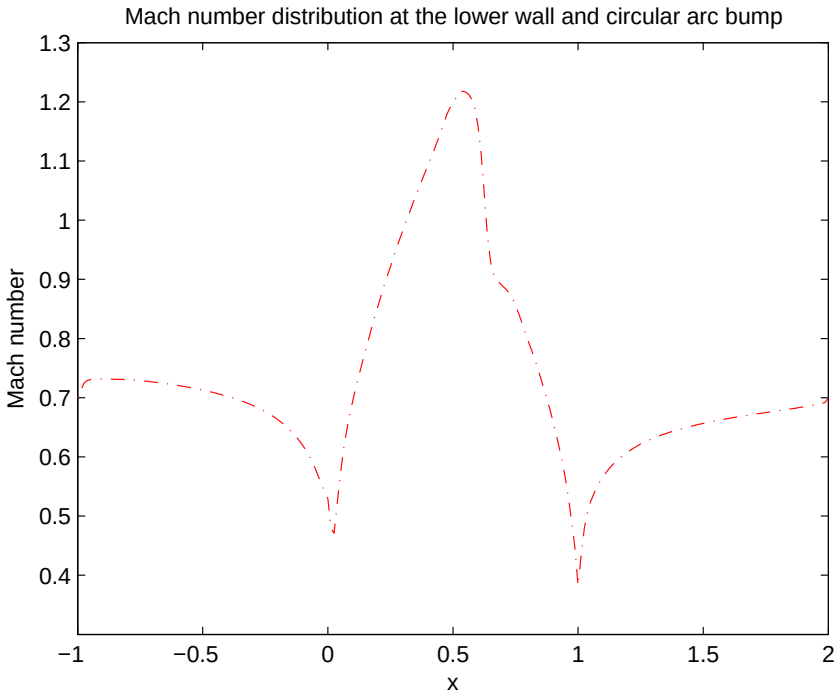

Figure 12. Mach number distribution for channel flow over a circular arc bump with 241 × 241 grid points at $y = 0$ and on the bump surface.

to the acceleration over the circular arc bump and reaches a minimum downstream of the maximum point of the bump. The shock is clearly visible in Fig. 11 and much sharper than with a 121 × 121 grid (not shown). We observe a pressure increase over the shock and towards the trailing edge and a subsequent decrease towards the outflow boundary. In Fig. 12 we show the distribution of the Mach number M for internal flow over the circular arc bump. We observe supersonic flow between $x \approx 0.3$ and $\approx 0.6m$. Again, the shock at $x \approx 0.6m$ is clearly visible.

Conclusions

In this work, we introduced a new approach to account for ghost points at embedded boundaries for the Cartesian grid method. At an embedded solid boundary we employ a simplified ghost point treatment in which the fluid point F is chosen on the vertical grid line through ghost point G adjacent to the boundary as the mirror point. We investigate the accuracy of the Cartesian grid method for the 2D compressible Euler equations simulating transonic flow over a circular arc bump. We use the local Lax-Friedrichs method and the MUSCL approach for spatial discretization. For time integration we use the third order TVD Runge-Kutta method. The Cartesian grid method needs a larger number of grid points than body fitted grid methods to get accurate results. In our Cartesian grid results, the location of the shock is upstream compared to the body-fitted grid result. Further grid refinement is expected to improve the shock location and the quantitative results. This expectation is supported by our observation that the simulated Mach numbers and the supersonic region get larger and closer to the body-fitted grid results when going from a coarse to a finer grid.

Acknowledgements

The current research has been funded by the Higher Education Commission (HEC) of Pakistan.

References

[1] A. Jameson, W. Schmidt and E. Turkel. Numerical solutions of the Euler equations by finite volume methods using Runge-Kutta time-stepping schemes. *AIAA Paper 81-1259*, 1981.

[2] E. Dick. A flux-difference splitting method for steady Euler equations. *Journal of Computational Physics*, 76(1): 19–32, 1988.

[3] E. Issman, G. Degrez and H. Deconinck. Implicit upwind residual-distribution Euler and Navier-Stokes solver on unstructured meshes. *AIAA Journal*, 34(10): 2021–2028, 1996.

[4] V. Venkatakrishnan and D.J. Mavriplis. Implicit method for the computation of unsteady flows on unstructured grids. *Journal of Computational Physics*, 127(2): 380–397, 1996.

[5] H . S. Udaykumar, S. Krishmann and S. V. Marella. Adaptively refined parallelised sharp interface Cartesian grid method for three dimensional moving boundary problem. *International Journal of Computational Fluid Dynamics*, 23(1): 1–24, 2009.

[6] B. Sjögreen and N. A. Petersson. A Cartesian embedded boundary method for hyperbolic conservation laws. *Communications in Computational Physics*, 2(6): 1199–1219, 2007.

[7] P. Colella, D. Graves, B. Keen and D. Modiano. A Cartesian grid embedded boundary method for hyperbolic conservation laws. *Journal of Computational Physics*, 211(1): 347–366, 2006

[8] R. Mittal, H. Dong, M. Bozkurttas, F. Najjar, A. Vargas and A. von Loebbecke. A versatile sharp interface immersed boundary method for incompressible flows with complex boundaries. *Journal of Computational Physics*, 227(10): 4825-4852, 2008.

[9] R. Löhner, J. Cebral, F. Camelli, S. Appanaboyina, J. Baum, E. Mestreau and O. Soto. Adaptive embedded and immersed unstructured grid techniques. *Comput.Methods Appl. Mech. Engrg*, 197(25-28): 2173–2197, 2008.

[10] D. Hartmann, M. Meinke and W. Schröder. A strictly conservation Cartesain cut-cell method for compressible viscous flows on adaptive grids *Comput.Methods Appl. Mech. Engrg*, 200(9-12) : 1038-1052, 2011.

[11] M. A. Farooq and B. Müller. A Cartesian grid method for compressible inviscid flows. *in: B. Skallerud, H. I. Andersson (Eds.), MekIT'11, Sixth National Conference on Computational Mechanics Trondheim, Norway, 23-24 May 2011*, 47–57, 2011.

[12] C. Hirsch. *Numerical computation of internal and external flows.* Elsevier, Amsterdam, 2007.

[13] B. van Leer. Towards the ultimate conservative difference scheme. V. A second-order sequel to Godunov 's method. *Journal of Computational Physics*, 32(1): 101-136, 1979.

[14] S. Gottlieb and C. Shu. Total variation diminishing Runge-Kutta schemes. *Mathematics of Computations*, 67(221): 73–85, 1998.

[15] B. Müller. Influence of inlet and outlet boundary conditions in internal flow computations at low Mach numbers. *in: Desideri,J.-A., Hirsch,C., Le Tallec,P., Pandolfi,M., Periaux,J. (Eds.), Computational Fluid Dynamics '96, Proceedings of 2nd ECCOMAS Congress, Paris, 9-13 Sept. 1996*, John Wiley, Chichester, 637–643, 1996.

M. Asif Farooq, B. Müller
Department of Energy and Process Engineering
Norwegian University of Science and Technology (NTNU)
Kolbjørn Hejes Vei 2 No-7491, Trondheim, Norway
asif.m.farooq@ntnu.no, bernhard.muller@ntnu.no